FINITE DIFFERENCE SCHEMES ON HEXAGONAL GRIDS FOR THIN LINEAR PLATES WITH FINITE VOLUME BOUNDARIES

Brian Hamilton, [*]
Acoustics and Audio Group,
University of Edinburgh
brian.hamilton@ed.ac.uk

Alberto Torin,
Acoustics and Audio Group,
University of Edinburgh
a.torin@sms.ed.ac.uk

ABSTRACT

The thin plate is a key structure in various musical instruments, including many percussion instruments and the soundboard of the piano, and also is the mechanism underlying electromechanical plate reverberation. As such, it is a suitable candidate for physical modelling approaches to audio effects and sound synthesis, such as finite difference methods—though great attention must be paid to the problem of numerical dispersion, in the interest of reducing perceptual artefacts. In this paper, we present two finite difference schemes on hexagonal grids for such a thin plate system. Numerical dispersion and computational costs are analysed and compared to the standard 13-point Cartesian scheme. An equivalent finite volume scheme can be related to the 13-point Cartesian scheme and a 19-point hexagonal scheme, allowing for fitted boundary conditions of the clamped type. Theoretical modes for a clamped circular plate are compared to simulations. It is shown that better agreement is obtained for the hexagonal scheme than the Cartesian scheme.

1. INTRODUCTION

The vibration of thin linear plates is a starting point for the modelling and sound synthesis of many musical systems, such as cymbals, gongs, stiff membranes, soundboards, and instrument bodies. Plate vibration is also important for plate reverberation as a digital audio effect. Among the various approaches adopted for the simulation of linear plates, modal techniques are an attractive option, and can be extended to non-linear equations as well [1, 2]. Finite difference and finite element methods have also been extensively adopted [3].

In the modelling of plates using finite difference methods, minimising numerical dispersion is critical, as it can introduce artefacts, such as a mistuning of modes and incorrect modal densities [4]. The latter effect is due to a loss of bandwidth in the simulations, giving rise to sparsity in frequencies leading to the Nyquist frequency. Numerical dispersion has been, and continues to be, extensively studied for the second-order wave equation [5, 6], but aside from [7], this topic has been neglected for the case of linear plates. Research has instead focused on simulating the non-linear aspects of plate vibration, which are arguably more interesting pursuits [8].

The regular hexagonal grid is an alternative to the regular Cartesian (square) grid in 2-D, and it has been shown to provide computationally efficient finite difference schemes for the second-order wave equation [6], mainly due to the isotropy of discrete Laplacians on the hexagonal grid [9]. It is thus of interest to study discrete biharmonic operators (bilaplacians) on the hexagonal grid, which, to our knowledge, have not been used for time-domain plate simulations. Aside from some sparse references found throughout the numerical methods and scientific computing literature [9, 10, 11, 12], relatively little research has featured the hexagonal discrete biharmonics that will be employed in this study.

This paper is organised as follows. In Section 2, the model equation for the plate is introduced and in Section 3, the hexagonal finite difference schemes are presented along with von Neumann stability conditions. In Section 4, numerical dispersion and computational efficiency are analysed. In Section 5, finite volume formulations are presented to implement boundary conditions, and stability conditions for the boundary value problem are given in terms of matrix eigenvalues. Section 6 features circular plate simulations in order to validate the numerical schemes. Conclusions and future directions of study are given in Section 7.

2. THIN PLATE VIBRATION

Linear lossless vibrations of plates are governed by the following equation [13]

$$\partial_t^2 w + \kappa^2 \Delta^2 w = 0\,, \tag{1}$$

where $w(t, \mathbf{x})$ represents the transverse displacement of the plate, t is time and $t \in \mathbb{R}^+$, $\mathbf{x} := (x, y) \in \mathbb{R}^2$ and Δ is the 2-D Laplacian operator, $\Delta := \partial_x^2 + \partial_y^2$, and thus Δ^2 is the biharmonic operator, or bilaplacian. The notation ∂_t denotes partial differentiation with respect to t, and similarly for ∂_x and ∂_y. κ is a constant defined by

$$\kappa = \sqrt{\frac{Ea^2}{12d(1-\nu^2)}}\,, \tag{2}$$

where d is the plate density in kg/m^3, a is the thickness in m, E is Young's modulus in Pa, and ν is the dimensionless Poisson's ratio. All of these parameters are positive.

Eq. (1) holds as long as the transverse displacement w is small in comparison with the thickness a (small deflections regime) [14], and is the 2-D analogue of the Euler-Bernouilli equation for a beam [13]. For deflections of the same order of magnitude as a, this linear equation no longer holds; some simplifying assumptions on the system must be dropped and a more complicated, non-linear equation must be taken into account (von Kármán-Föppl equations [15]).

[*] This work was supported by the European Research Council, under grant StG-2011-279068-NESS, and by the Natural Sciences and Engineering Research Council of Canada.

3. NUMERICAL SCHEME

3.1. Temporal and spatial grids

We discretise time with the temporal grid $\mathbb{T} := \{nk, n \in \mathbb{Z}^+\}$, where k is the time-step. Space will be discretised with a spatial grid $\mathbb{G}$ which is either a square (Cartesian) grid: $\mathbb{G}_C := h\mathbb{Z}^2$ or a hexagonal grid $\mathbb{G}_H$ defined by

$$\mathbb{G}_H := \{h\mathbf{V}\mathbf{z} \in \mathbb{R}^2, \mathbf{z} \in \mathbb{Z}^2\}\,, \quad \mathbf{V} = \begin{bmatrix} 1 & -1/2 \\ 0 & \sqrt{3}/2 \end{bmatrix}. \quad (3)$$

3.2. Difference operators

Let $\hat{w}(t, \mathbf{x})$ represent an approximation to the solution of interest $w(t, \mathbf{x})$. A temporal shift operator may be defined as

$$s_{t\pm}\hat{w} := \hat{w}(t \pm k, \mathbf{x})\,, \quad (4)$$

and a centered time-difference operator can then be written as

$$\delta_{tt} := \frac{1}{k^2}\left(s_{t+} - 2 + s_{t-}\right) = \partial_t^2 + O(k^2)\,. \quad (5)$$

Let us define the spatial shift operator

$$s_{\mathbf{r},h}\hat{w} := \hat{w}(t, \mathbf{x} + \mathbf{r}h) \quad (6)$$

where $\mathbf{r} \in \mathbb{R}^2$. The simplest discrete Laplacian on the regular Cartesian grid is then

$$\delta_{C,\Delta} := \frac{1}{h^2}\sum_{\mathbf{r}\in\Omega_C}\left(s_{\mathbf{r},h} - 1\right) = \Delta + O(h^2)\,, \quad (7)$$

where Ω_C is the set of four unit vectors in $\mathbb{Z}^2$. On the hexagonal grid we consider the following two discrete Laplacians

$$\delta_{H,\Delta} := \frac{2}{3h^2}\sum_{\mathbf{r}\in\Omega_H}\left(s_{\mathbf{r},h} - 1\right) = \Delta + \frac{1}{16}h^2\Delta^2 + O(h^4)\,, \quad (8)$$

$$\delta^*_{H,\Delta} := \frac{2}{9h^2}\sum_{\mathbf{r}\in\Omega^*_H}\left(s_{\mathbf{r},h} - 1\right) = \Delta + \frac{3}{16}h^2\Delta^2 + O(h^4)\,, \quad (9)$$

where Ω_H and Ω^*_H are the sets of six vectors with norms h and $\sqrt{3}h$ in $\mathbb{G}_H$ respectively. These discrete Laplacians on their respective grids are illustrated in Fig. 1.

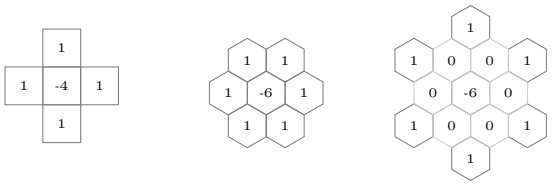

(a) $\delta_{C,\Delta}$ (b) $\frac{3}{2}\delta_{H,\Delta}$ (c) $\frac{9}{2}\delta^*_{H,\Delta}$

Figure 1: Stencil weights for discrete Laplacians, scaled by h^2

Now we can construct discrete biharmonics by the composition of discrete Laplacians in the following manner

$$\delta_{C,\Delta^2} := (\delta_{C,\Delta})^2 = \Delta^2 + O(h^2)\,, \quad (10)$$

$$\delta_{H,\Delta^2} := (\delta_{H,\Delta})^2 = \Delta^2 + \frac{1}{8}h^2\Delta^3 + O(h^4)\,. \quad (11)$$

The Cartesian biharmonic δ_{C,Δ^2} is a stencil that employs 13 points. The second-order error in (10) is anisotropic so it is not displayed. The hexagonal biharmonic δ_{H,Δ^2} is a 19-point stencil, and has an isotropic second-order error term (the triharmonic operator), which is due to the isotropic second-order error term in $\delta_{H,\Delta}$.

Another biharmonic on the hexagonal grid, using only 13 points [9], can be written as a linear combination of $\delta_{H,\Delta}$ and $\delta^*_{H,\Delta}$:

$$\delta^\star_{H,\Delta^2} := \frac{8}{h^2}(\delta^*_{H,\Delta} - \delta_{H,\Delta}) = \Delta^2 + O(h^2)\,. \quad (12)$$

This discrete biharmonic is different from δ_{C,Δ^2} and δ_{H,Δ^2} in that it cannot be decomposed into the composition of two discrete Laplacians. The three discrete biharmonics are shown on their respective grids in Fig. 2.

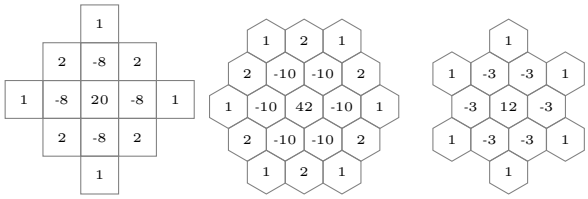

(a) δ_{C,Δ^2} (b) $\frac{9}{4}\delta_{H,\Delta^2}$ (c) $\frac{9}{16}\delta^\star_{H,\Delta^2}$

Figure 2: Stencil weights for discrete biharmonics, scaled by h^4 .

3.3. Finite difference schemes

Combining these operators gives three finite difference schemes for (1)

$$\delta_{tt}\hat{w} + \kappa^2\delta_{\Delta^2}\hat{w} = 0\,, \quad (t, \mathbf{x}) \in \mathbb{T} \times \mathbb{G}\,, \quad (13)$$

with possible choices of $\delta_{\Delta^2} \in \{\delta_{C,\Delta^2}, \delta_{H,\Delta^2}, \delta^\star_{H,\Delta^2}\}$ and its appropriate spatial grid $\mathbb{G} \in \{\mathbb{G}_C, \mathbb{G}_H\}$. Each scheme has the time recursion

$$\hat{w}^+ = (2 - \mu^2\delta^h_{\Delta^2})\hat{w} - \hat{w}^-\,, \quad (14)$$

where $\hat{w}^\pm := s_{t\pm}\hat{w}$, $\mu := \kappa k/h^2$ is a free parameter to be set, analogous to the Courant number in wave equation schemes, and $\delta^h_{\Delta^2} := h^4\delta_{\Delta^2}$. The recursion begins from the two known (or approximated) values $\hat{w}(0, \mathbf{x})$ and $\hat{w}(k, \mathbf{x})$ determined from the initial conditions. Note that this explicit update is parallelisable, and thus, well-suited to GPU implementations [16].

3.4. Stability analysis

To determine stability conditions, we can take the Z-transform of (13) to get the following quadratic equation in $z \in \mathbb{C}$

$$z + \mu^2\Lambda - 2 + z^{-1} = 0\,, \quad (15)$$

where $\Lambda = \Lambda(\boldsymbol{\xi})$ is the Fourier symbol of the operator $\delta^h_{\Delta^2}$ and $\boldsymbol{\xi} \in \mathbb{R}^2$ are the spatial frequencies. For now, we assume that $\Lambda(\boldsymbol{\xi})$ has the property $\Lambda \geq 0$. A stability condition (disallowing exponential growth) is found from the condition $|z| \leq 1$, which leads to

$$\mu \leq \mu_{\max} := \sqrt{4/\Lambda_{\max}}\,, \quad (16)$$

where $\Lambda_{\max} := \max_{\boldsymbol{\xi}}\Lambda$ for the spatial frequencies $\boldsymbol{\xi} \in \mathbb{R}^2$. For the three biharmonics $\delta_{C,\Delta^2}, \delta_{H,\Delta^2}, \delta^\star_{H,\Delta^2}$ (scaled by h^4) we have respectively

$$\Lambda_{C,\max} = 64\,, \quad \Lambda_{H,\max} = 36\,, \quad \Lambda^\star_{H,\max} = 48\,. \quad (17)$$

The first two values are given by previous studies [11], and the latter can be found by examining $\Lambda^{\star}_{H,\max}$. Stability limits for the schemes in (13) are respectively

$$\mu_{C,\max} = 1/4\,, \quad \mu_{H,\max} = 1/3\,, \quad \mu^{\star}_{H,\max} = \sqrt{1/12}\,. \tag{18}$$

Note that both of the hexagonal schemes give higher $\mu_{\max}$ than the Cartesian scheme, which allows for a larger time-step when h is fixed. On the other hand, if k is fixed to $k = 1/F_s$, as is common in sound synthesis applications, this implies a smaller minimum grid spacing (spatial step). Setting h as small as possible is generally a good choice for numerical dispersion and maximising the temporal bandwidth in the approximation [4]. However, this also increases the density of the spatial grid, and the hexagonal grid is already $2/\sqrt{3} \approx 1.15$ times more dense than the square grid for the same h. More will be said about this in Section 4.1.

4. NUMERICAL DISPERSION

The dispersion relation for our plate equation is

$$\omega = \pm\kappa|\boldsymbol{\xi}|^2\,, \tag{19}$$

where $\omega \in \mathbb{R}$ represents the temporal frequency in rad/s and $|\boldsymbol{\xi}|$ is the *wavenumber* in rad/m. The plate system is dispersive, as seen by its phase velocity:

$$v_\phi = \kappa|\boldsymbol{\xi}|\,. \tag{20}$$

In other words, plane-waves with small wavenumbers travel slower than plane-waves with large wavenumbers.

In order to analyse numerical dispersion of the finite difference scheme it helps to define a normalised spatial frequency $\boldsymbol{\xi}_h := \boldsymbol{\xi}h$ and a normalised frequency $\omega_k := \omega k$. We can then write the Fourier symbol for each discrete Laplacian $\delta_{C,\Delta}, \delta_{H,\Delta}, \delta^{*}_{H,\Delta}$, scaled by h^2, as

$$\Gamma_C(\boldsymbol{\xi}_h) := -2\sum_{\mathbf{r}\in\Omega_C} \sin^2(\boldsymbol{\xi}_h\cdot\mathbf{r}/2)\,, \tag{21a}$$

$$\Gamma_H(\boldsymbol{\xi}_h) := -\frac{4}{3}\sum_{\mathbf{r}\in\Omega_H} \sin^2(\boldsymbol{\xi}_h\cdot\mathbf{r}/2)\,, \tag{21b}$$

$$\Gamma^{*}_H(\boldsymbol{\xi}_h) := -\frac{4}{9}\sum_{\mathbf{r}\in\Omega^{*}_H} \sin^2(\boldsymbol{\xi}_h\cdot\mathbf{r}/2)\,. \tag{21c}$$

This allows us to build Λ_C, Λ_H, $\Lambda^{\star}_H$ as follows

$$\Lambda_C = (\Gamma_C)^2\,, \quad \Lambda_H = (\Gamma_H)^2\,, \quad \Lambda^{\star}_H = 8(\Gamma^{*}_H - \Gamma_H)\,. \tag{22}$$

Clearly, Λ_C and Λ_H are non-negative. Examining $\Lambda^{\star}_H$ gives the same result, but we leave this out for brevity. We can then write the *relative phase velocity* as

$$v_{\text{rel}}(\boldsymbol{\xi}_h) := \frac{\omega_k(\boldsymbol{\xi}_h)}{\mu|\boldsymbol{\xi}_h|^2}\,, \quad \omega_k(\boldsymbol{\xi}_h) := 2\arcsin\left(\frac{\mu}{2}\sqrt{\Lambda}\right)\,, \tag{23}$$

for $\omega_k \in (0,\pi]$ and $\boldsymbol{\xi}_h \in \mathbb{B}$, where $\mathbb{B}$ is the wavenumber cell of the grid. For the square grid, $\mathbb{B}$ is a square centered at zero with sides of length 2π, whereas for the hexagonal grid, $\mathbb{B}$ is the Voronoi cell (a hexagon) of the lattice spanned by the vectors:$(2\pi, 2\pi/\sqrt{3})^T$ and $(0, 4\pi/\sqrt{3})^T$ [6]. The relative phase velocity should ideally be unity everywhere. Figs. 3(a)-(c) display the relative phase velocities of the finite difference schemes with $\mu = \mu_{\max}$. Note that the hexagonal wavenumber cell is slightly bigger than the Cartesian wavenumber cell, this is ultimately a result of the denser grid for the same h. Also, the isotropic characteristic to δ_{H,Δ^2} can be seen in Fig. 3b. Some simulations, without taking boundaries into account, are presented in Fig. 4 to demonstrate how the directional dependence of the schemes are reflected in the numerical approximation. The initial conditions $\hat{w}(0,\mathbf{x})$ and $\hat{w}(k,\mathbf{x})$ are set to a spatial Gaussian for each case, and the simulations are stopped at the same time instant. It is clear that the approximation in Fig. 4b has less directional dependence than the other two.

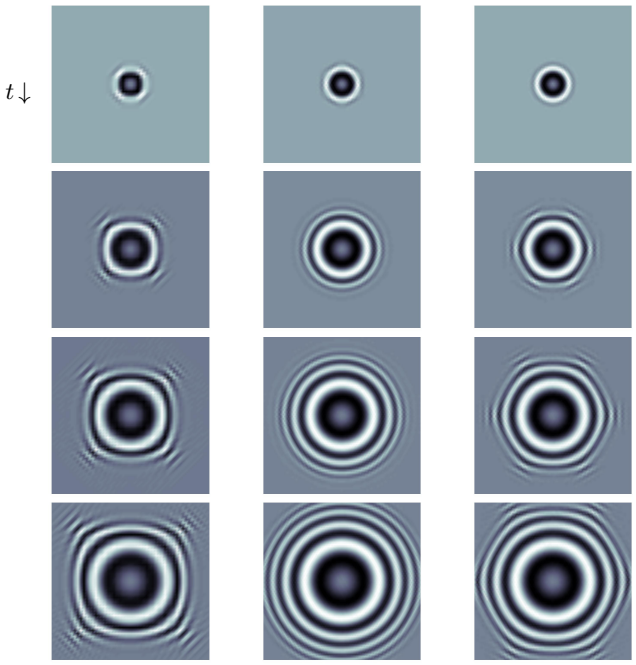

(a) 13-pt Cartesian (b) 19-pt hexagonal (c) 13-pt hexagonal

Figure 4: Spatial response to same initial conditions (Gaussian), demonstrating (an)isotropy. Time-step fixed across schemes. Snapshots after 9, 18, 27, and 36 time-steps (top to bottom).

We would like to compare the dispersion for the Cartesian scheme to the hexagonal schemes, but this can be difficult since they are defined in different wavenumber cells. To make for a better comparison we can use the dispersion relation to reassign the relative phase velocities to ω_k and an angle of propagation $\theta \in [0, 2\pi]$, giving a function $v_{\text{rel}}(\omega_k(\boldsymbol{\xi}_h), \theta(\boldsymbol{\xi}_h))$ where

$$\theta(\boldsymbol{\xi}_h) = \arctan\left((\boldsymbol{\xi}_h\cdot\hat{\mathbf{y}})/(\boldsymbol{\xi}_h\cdot\hat{\mathbf{x}})\right)\,. \tag{24}$$

where $\hat{\mathbf{x}}, \hat{\mathbf{y}}$ are the standard unit vectors in $\mathbb{R}^2$. Now we have a single domain on which to compare relative phase velocities for the Cartesian and hexagonal schemes. These relative phase velocities, are displayed in Figs. 3(d-e).

It is from this point of view (temporal frequencies) that we see large variations between the schemes. There are two effects of numerical dispersion that are prevalent here. The first is that the high spatial frequencies are compressed into a small band of temporal frequencies along the worst-case directions (multiples of $\pi/2$ for the Cartesian scheme, odd multiples of $\pi/6$ for hexagonal schemes). This will cause an unnatural modal density within those bands of frequencies. The second effect is that the spatial Nyquist

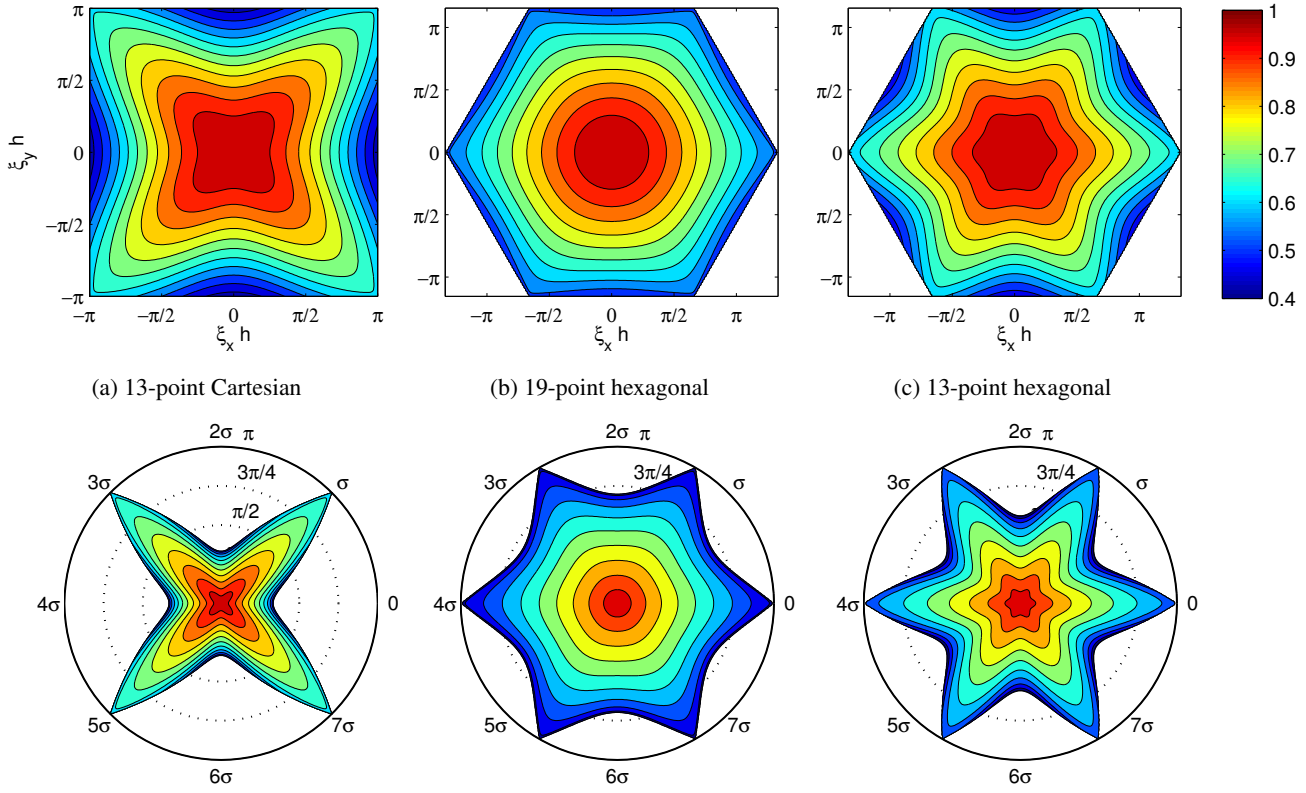

(a) 13-point Cartesian (b) 19-point hexagonal (c) 13-point hexagonal

(d) 13-point Cartesian (e) 19-point hexagonal (f) 13-point hexagonal

Figure 3: Contour plots of relative phase velocity as a function of $\boldsymbol{\xi}_h \in \mathbb{B}$, ($\boldsymbol{\xi}_h = (\xi_x h, \xi_y h)$) (top row), and $\omega_k \in [0, \pi]$ (radial) and $\theta \in [0, 2\pi]$ (bottom row), where $\sigma = \pi/4$. Contours mark 5% deviations in relative phase velocity.

does not remap to the temporal Nyquist in every direction, creating directional *cutoff frequencies*. Thus, above the smallest directional cutoff frequencies the modal density will be incorrect. These effects are worst in the Cartesian scheme, while the 19-point hexagonal scheme experiences the least of these effects.

4.1. Normalising for computational cost

It can be argued that this is still not a fair comparison between Cartesian and hexagonal schemes, since δ_{H,Δ^2} uses 19 spatial points instead of 13 for δ_{C,Δ^2}. Furthermore, for a fixed time-step (fixed sample rate) and $\mu = \mu_{\max}$ the hexagonal grid will be more dense than the Cartesian one. This ultimately leads to more computation per unit time and space. In principle, it is always possible to oversample the grid in order to achieve the same levels of accuracy or simulated bandwidth with the 13-point Cartesian scheme, so we have to somehow normalise for computational costs.

Three different methods can be adopted to evaluate the finite difference schemes. First, we will consider the same time-step for each scheme (no normalisation of computational cost), then we will normalise for spatiotemporal grid ($\mathbb{T} \times \mathbb{G}$) densities, and finally we will consider normalised spatiotemporal densities of addition operations.

Let the time-step for each scheme be set to $k = \chi k'$, where k' is a constant and χ will represent computational cost normalisation factors with respect to the Cartesian scheme. As such, χ is always set as $\chi = 1$ for the Cartesian scheme. When $\chi = 1$ for all schemes, normalisation for computational cost is ignored. On the other hand, when χ is chosen as $\chi = \sqrt{4\eta\mu}$ with $\eta = 1$ for the Cartesian scheme and $\eta = 2/\sqrt{3}$ for the hexagonal schemes, then we have normalised for density of points in space and time, with respect to the Cartesian scheme. When $\chi = \sqrt{(4/13)\gamma\eta\mu}$, where γ is the number of points in the stencil, then the schemes will be normalised for the density of additions per space and time, with respect to the Cartesian scheme. We neglect multiplications for brevity.

The relative phase velocities with these normalisations along the respective worst-case directions are shown in Fig. 5. It can be seen that, even after normalising for the extra computational costs, the hexagonal schemes are more efficient at reducing numerical dispersion than the Cartesian scheme. In parallel implementations of finite difference schemes for plates, such as [17], the normalisation for additions, which are easily parallelised, may not be important so we ignore this normalisation for the following discussion.

For the plate problem, reducing the time-step results in a squared increase in the total number of operations (2x increase in F_s equals 4x computational cost). With this in mind, we can compare schemes in terms of a *relative computational efficiency* to attain a certain accuracy in the relative phase velocity up to a given frequency, as in [5] for wave equation schemes. For example, with data taken from Fig. 5, we can calculate that the 19-point and 13-point hexagonal schemes are respectively 2.1 and 1.8 times more efficient than the 13-point Cartesian scheme for a one-percent rela-

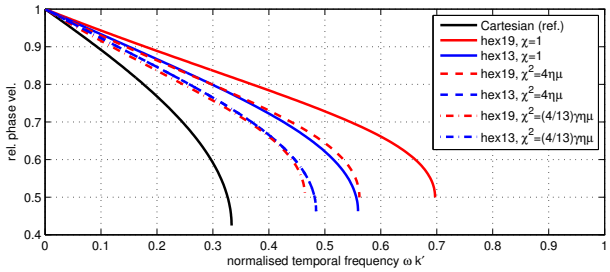

Figure 5: Relative phase velocity along worst-case direction for three schemes, with various normalisations for computational cost. The time-step in each case is set as $k = \chi k'$ for k' fixed, so $\chi = 1$ implies no normalisation (same time-step), $\chi^2 = 4\eta\mu$ normalises for spatiotemporal grid densities, and $\chi^2 = (4/13)\gamma\eta\mu$ normalises for spatiotemporal density of additions. Note, $\gamma = 13$ for the 13-point hexagonal scheme, so the $\chi^2 = 4\eta\mu$ and $\chi^2 = (4/13)\gamma\eta\mu$ curves overlap.

tive phase velocity error tolerance. Such relative efficiency numbers could be given for the entire range of phase velocity errors, but it is unknown how much numerical dispersion is tolerated for audio applications of this plate model, and whether numerical dispersion is perceptually distinguishable from the system's underlying dispersion.

Perhaps a more useful comparison is in terms of the global cutoff frequencies after normalisation, as this gives an idea of the modal density across the temporal range of frequencies, and thus a measure of how 'rich' the output sound will be. In terms of global cutoff frequencies, we can calculate that the 19-point and 13-point hexagonal schemes are respectively 4.3 and 2.8 times more efficient than the 13-point Cartesian scheme.

5. FINITE VOLUME BOUNDARIES

In this section, we present a finite volume formulation of the 13-point Cartesian scheme and the 19-point hexagonal scheme, in order to simplify the implementation of certain boundary conditions. The 13-point discrete biharmonic on the hexagonal grid does not decompose into the composition two discrete Laplacians, so it cannot be easily be interpreted within the following finite volume framework.

Let $\mathcal{V}$ denote a closed 2-D volume and $\partial\mathcal{V}$ its boundary. The finite grid under consideration can then be written as $\overline{\mathbb{G}} := \mathbb{G} \cap \mathcal{V}$. We start by rewriting (1) as the system of two equations:

$$\partial_t v = \kappa \Delta m \,, \tag{25a}$$

$$\partial_t m = -\kappa \Delta v \,, \tag{25b}$$

where $m = m(t, \mathbf{x})$ is the initial moment and $v = v(t, \mathbf{x})$ is the initial velocity, which is related to w by:

$$v = \partial_t w \tag{26}$$

In this system, the two initial conditions to specify are $v(0, \mathbf{x})$ and $m(0, \mathbf{x})$. Boundary conditions for the plate can be of the clamped type:

$$v = \mathbf{n} \cdot \nabla v = 0 \,, \quad \mathbf{x} \in \partial\mathcal{V} \tag{27}$$

where $v = 0$ denotes a homogeneous Dirichlet condition and $\mathbf{n} \cdot \nabla v = 0$ denotes a homogeneous Neumann boundary condition. Another set of Dirichlet boundary conditions is the following:

$$v = m = 0 \,, \quad \mathbf{x} \in \partial\mathcal{V} \,. \tag{28}$$

This set of conditions may be a simplified form of the "simply supported" conditions for certain geometries, such as rectangular plates with Cartesian grids.

Consider a tiling of closed cells $\mathcal{C}_i$ whose interiors are pairwise disjoint, and the tiling fills up the volume $\mathcal{V}$, i.e. $\bigcup_i \mathcal{C}_i = \mathcal{V}$. Now consider one cell surrounding some point $\mathbf{x}_i \in \overline{\mathbb{G}}$. For now we will focus on one of the two equations, as they are similar. Integrating both sides of (25a) over the volume of the cell and applying the divergence theorem we have:

$$\int_{\mathcal{C}_i} \partial_t v \, dS = \kappa \int_{\partial\mathcal{C}_i} \mathbf{n} \cdot \nabla m \, dr \,, \tag{29}$$

where $\partial\mathcal{C}_i$ denotes the *boundary of* $\mathcal{C}_i$ and where $\mathbf{n}$ is the normal vector pointing out of the cell at $r \in \mathcal{C}_i$. Now, consider that this cell has neighbouring cells $\mathcal{C}_j$ with indices j in the set of neighbour indices N_i. The interiors of cells are pairwise disjoint but their closures can intersect. Let these intersections be denoted by $\mathcal{S}_{ij} := \mathcal{C}_i \cap \mathcal{C}_j$; these are the sides of the cell. Furthermore, let $\mathcal{S}_{i(b)} := \mathcal{C}_i \cap \partial\mathcal{V}$ denote the boundary side of the cell. Since $\partial\mathcal{C}_i = (\bigcup_j \mathcal{S}_{ij}) \cup \mathcal{S}_{i(b)}$ we can write (29) as

$$\int_{\mathcal{C}_i} \partial_t v \, dS = \kappa \sum_{j \in N_i} \int_{\mathcal{S}_{ij}} \mathbf{n} \cdot \nabla m \, dr + \kappa \int_{\mathcal{S}_{i(b)}} \mathbf{n} \cdot \nabla m \, dr \,, \tag{30}$$

The last term describes one half of the system at the boundary and this can be set to zero for Neumann conditions. Let the 2-D volume (area) of the cell be V_i and the length of each side be S_{ij} and similarly for the boundary side $S_{i(b)}$. We define the first-order spatial and time differences:

$$\delta_{t\pm} := \pm \frac{1}{k} (s_{t\pm} - 1) \,, \tag{31a}$$

$$\delta_{ij} \hat{w}_j := \frac{1}{h_{ij}} (\hat{w}_j - \hat{w}_i) \,, \tag{31b}$$

where $h_{ij} = \|\mathbf{x}_j - \mathbf{x}_i\|$. Consider the variables $\hat{v}_i := \hat{v}(t + k/2, \mathbf{x}_i)$ and $\hat{m}_i := \hat{m}(t, \mathbf{x}_i)$, representing approximations to $v(t + k/2, \mathbf{x}_i)$ and $m(t, \mathbf{x}_i)$ respectively. Neglecting for now the boundary term, we can approximate (30) with the following, and (25b) by the same procedure:

$$V_i \delta_{t-} \hat{v}_i = \kappa \sum_{j \in N_i} S_{ij} \delta_{ij} \hat{m}_i \,, \tag{32a}$$

$$V_i \delta_{t+} \hat{m}_i = -\kappa \sum_{j \in N_i} S_{ij} \delta_{ij} \hat{v}_i \,. \tag{32b}$$

Note that the time differences are centered, since $\hat{v}_i$ is staggered in time. The spatial difference will also be centered about the sides of the cells for the grids (square and hexagonal) considered here. Now rearranging for the update equations we have:

$$\hat{v}_i = \hat{v}_i^- + \frac{\kappa k}{V_i} \sum_{j \in N_i} S_{ij} \delta_{ij} \hat{m}_i \,, \tag{33a}$$

$$\hat{m}_i^+ = \hat{m}_i - \frac{\kappa k}{V_i} \sum_{j \in N_i} S_{ij} \delta_{ij} \hat{v}_i \,, \tag{33b}$$

where $\hat{v}_i^- := s_{t-} \hat{v}_i$ and $\hat{m}_i^+ := s_{t+} \hat{m}_i$. The update does not change when Neumann conditions are applied because the neglected boundary term would be set to zero. For the clamped conditions, it then suffices to fix $\hat{v}_i = 0$ when $S_{i(b)} > 0$. For

the conditions (28), we also fix $\hat{m}_i^+ = 0$ when $S_{i(b)} > 0$. If, on the other hand, we update both values at the boundaries, then this implies the non-physical, yet well-posed, boundary conditions:

$$\mathbf{n} \cdot \nabla m = \mathbf{n} \cdot \nabla v = 0\,, \quad \mathbf{x} \in \partial\mathcal{V}\,. \tag{34}$$

We include this boundary condition because it arises naturally from the finite volume framework and it may provide interesting artificial reverberation.

To establish the link with the finite difference schemes, we will now consider square and regular hexagonal tilings of $\mathcal{V}$. These tilings may be *locally irregular* [18], which means that cells on the interior are regular polygons from the Voronoi tessellations of $\mathbb{G}_C$ or $\mathbb{G}_H$, but cells that intersect with the boundary of $\mathcal{V}$ may be irregular. Now consider a cell $\mathcal{C}_i$ with $S_{i(b)} = 0$ and $S_{j(b)} = 0$ for $j \in N_i$. It is straightforward to show [19] that we can recover the following discrete Laplacians from the finite volume formulations:

$$\frac{1}{V_i} \sum_{j \in N_i} S_{ij} \delta_{ij} \hat{v}_i = \delta_{C,\Delta} \hat{v}_i\,, \quad \mathbf{x}_i \in \mathbb{G}_C\,, \tag{35a}$$

$$\frac{1}{V_i} \sum_{j \in N_i} S_{ij} \delta_{ij} \hat{v}_i = \delta_{H,\Delta} \hat{v}_i\,, \quad \mathbf{x}_i \in \mathbb{G}_H\,. \tag{35b}$$

Then, using the identity $\delta_{t+}\delta_{t-}\hat{v}_i = \delta_{tt}\hat{v}_i$, it follows that Eqs. (32a) and (32b) simplify to the second-order 13-point Cartesian and 19-point hexagonal schemes respectively in $\hat{v}_i$. The variable $\hat{w}_i^+$ can be recovered from $\hat{v}_i = \delta_{t+}\hat{w}_i$.

5.1. Matrix formulation and stability

The approximations $\hat{v}$ and $\hat{m}$ can be written as the $N \times 1$ vectors $\mathbf{v}$ and $\mathbf{m}$ with the values of $\hat{v}_i$ and $\hat{m}_i$ for $\mathbf{x}_i \in \overline{\mathbb{G}}$ ($N = |\overline{\mathbb{G}}|$) at a particular time t. The system (32) can be rewritten in the matrix-vector form:

$$\delta_{t-}\mathbf{v} = \quad \kappa \mathbf{L}_1 \mathbf{m}\,, \tag{36a}$$

$$\delta_{t+}\mathbf{m} = -\kappa \mathbf{L}_2 \mathbf{v}\,, \tag{36b}$$

where $\mathbf{L}_1$ and $\mathbf{L}_2$ are $N \times N$ matrices corresponding to δ_Δ with Dirichlet conditions possibly imposed. These matrices can be defined as follows. Consider $\mathbf{L}$ to be either $\mathbf{L}_1$ or $\mathbf{L}_2$. For each row i of the matrix $\mathbf{L}$, the entries l_{ij} can be written as:

$$l_{ij} = \frac{S_{ij}}{V_i h_{ij}}\,, \quad i \neq j\,, \tag{37a}$$

$$l_{ii} = -\sum_{i \neq j} l_{ij}\,. \tag{37b}$$

In order to impose Dirichlet conditions, $\mathbf{L}$ must be modified on rows pertaining to boundary nodes. To impose the condition $v = 0$, we set $l_{ij} = 0$ in $\mathbf{L}_1$ when $S_{i(b)} > 0$. Similarly, to impose the condition $m = 0$, we set $l_{ij} = 0$ in $\mathbf{L}_2$ when $S_{i(b)} > 0$. If the boundary condition is (34), then $\mathbf{L}_1 = \mathbf{L}_2$.

Stability of the system (36) can be checked as follows. Recombining the system into one variable, we have

$$\mathbf{v}^+ = (2\mathbf{I} - \mu^2 \mathbf{B})\mathbf{v} - \mathbf{v}^-\,, \tag{38}$$

where $\mathbf{v}^\pm := s_{t\pm}\mathbf{v}$, $\mathbf{B} = h^4 \mathbf{L}_1 \mathbf{L}_2$, and where $\mathbf{I}$ is the $N \times N$ identity matrix. Here, h represents the minimum h_{ij} with $j \in N_i$ ($i \neq j$) and $\mathbf{x}_i \in \overline{\mathbb{G}}$. Similarly to the stability analysis presented for the initial value problem, we have the following "matrix method" [20] type stability condition

$$\mu \leq \sqrt{4/\rho(\mathbf{B})}\,, \tag{39}$$

provided that $\mathbf{B}$ is positive semi-definite (PSD), and where $\rho(\mathbf{B})$ denotes the spectral radius of $\mathbf{B}$. That $\mathbf{B}$ is PSD follows from (37) and Gerschgorin's theorem [21]. It is assumed that the tiling is constructed such that $\rho(\mathbf{B}) \leq \Lambda_{\max}$, and thus $\mu = \mu_{\max}$ (as given previously) will be sufficient for stability. Energy methods [19] should be employed to get a more instructive stability condition for the finite-volume meshing pre-processing step, but these will be left for a future study.

6. SIMULATIONS

6.1. Modes of clamped circular plate

In order to validate these schemes, we simulate a clamped circular plate with tabulated values for the modal frequencies from [22]. The circular plate of interest has a radius of one metre and $\kappa = 20$. The time-step is set to $k = 1/F_s$ where $F_s = 8000$ Hz for the Cartesian scheme, and $F_s = 6300$ Hz for the hexagonal scheme in order to (approximately) normalise for the spatiotemporal density of points. For both schemes we employ a "staircase" approximation and a "fitted" approximation to the circular domain. These tilings are shown in Fig. 6.

A normalised Kronecker delta (in space and time) is used as an excitation for the plate. The spectra of the resulting impulse responses, for low frequencies, are shown in Fig. 7. It can be observed that the fitted approximations are better than their staircase counterparts in both cases (Cartesian and hexagonal). However, as numerical dispersion is significant in both cases the modes are misrepresented above 250 Hz. We can also observe that in the Cartesian case, certain modal frequencies are in numerically split degenerate mode pairs (e.g. at 220 Hz and 270 Hz). This is a consequence of anisotropy, and it is clear that the hexagonal scheme offers an improvement in this respect.

6.2. Modal density and cutoff frequencies

Next we demonstrate the effects of the minimum directional cutoff frequencies, as discussed in Section 4. In Fig. 8, the same impulse responses are plotted, but now over the entire range of simulated temporal frequencies. The minimum cutoff frequencies are denoted with vertical dashed lines. These refer to $0.33F_s$ for the Cartesian scheme, and $0.70F_s$ for the hexagonal scheme.

For the Cartesian case in Fig. 8a, we can see the sparsity of modes increases above the (minimum) cutoff frequency, leading up to the maximum cutoff frequency (the Nyquist). As seen in Fig. 8b, the hexagonal scheme (normalised for computational cost) has a higher cutoff frequency and one can notice that the density of modes near 2000 Hz is greater than in the Cartesian case. With a 8000 Hz sample rate, in Fig. 8c, the hexagonal scheme provides a richer spectrum, albeit at a higher computational cost. For these simulations μ was set to $\mu_{\max}$ and (39) was satisfied.

Finally, we show the hexagonal circular plate with double Dirichlet conditions (28) and the double Neumann conditions (34). The spectra that were obtained are shown in Fig. 9. It can be seen that these conditions provide spectra qualitatively similar to the clamped conditions.

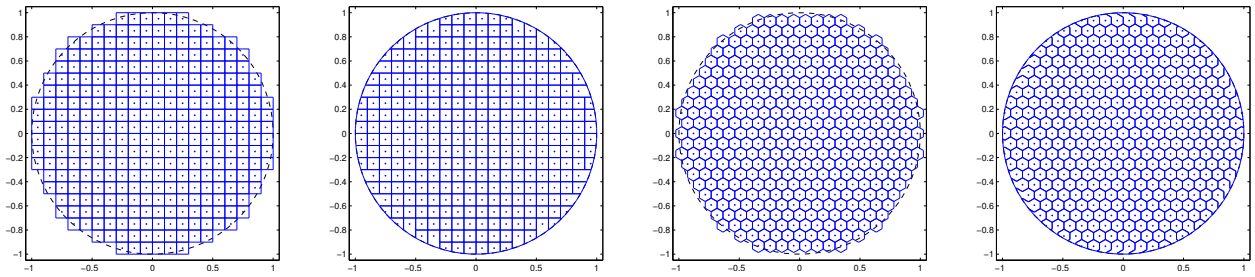

(a) Square, staircase (b) Square, fitted (c) Hexagonal, staircase (d) Hexagonal, fitted

Figure 6: Finite volume tilings representing circular plate of radius one. Square and hexagonal staircase and fitted tilings.

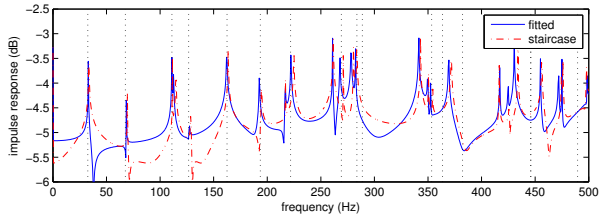

(a) Cartesian grid, $F_s = 8000$ Hz

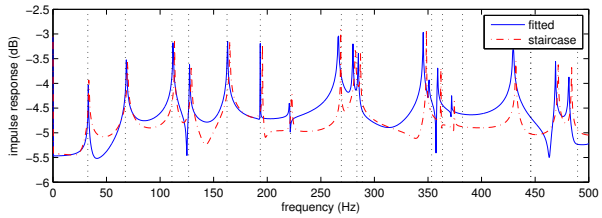

(b) Hexagonal grid, $F_s = 6300$ Hz

Figure 7: Impulse responses and analytical modes (dotted lines) of clamped circular plate

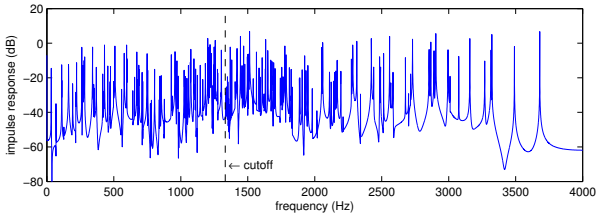

(a) Cartesian grid, $F_s = 8000$ Hz

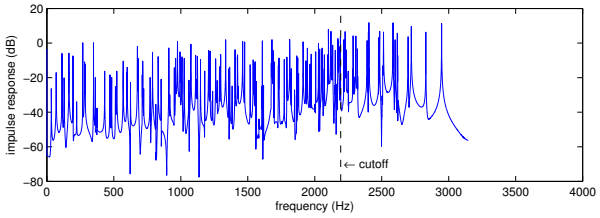

(b) Hexagonal grid, $F_s = 6300$ Hz

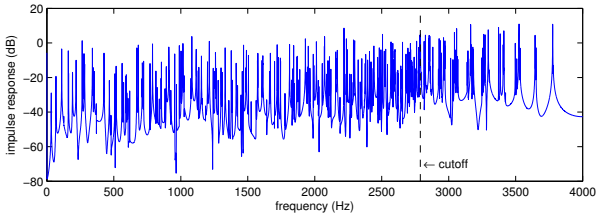

(c) Hexagonal grid, $F_s = 8000$ Hz

Figure 8: Comparison of spectra, clamped circular plate

7. CONCLUSIONS

In this paper, we have presented two finite difference schemes for thin plate vibration using hexagonal grids. Stability conditions were presented and numerical dispersion was analysed. It was shown that better computational efficiency in terms of minimising numerical dispersion can be achieved using hexagonal grids rather than Cartesian (square) grids. Equivalent finite volume schemes were presented for the 13-point Cartesian and 19-point hexagonal finite difference schemes in order to implement clamped boundary conditions over irregular geometries. Simulations of clamped circular plates were presented and it was seen that finite volume grids that conformed to the domain were more accurate than "staircase" approximations. Furthermore, modal accuracy was generally better with the hexagonal scheme for a comparable computational cost with the Cartesian scheme.

One issue that will be addressed in future work is a more thorough analysis of boundary conditions. The system (25) is but a simplified version of a more complex system involving bending and twisting moments [13], which naturally leads to the correct boundary conditions in the simply supported and free case. This complete system is arguably more difficult to simulate with unstructured grids within a finite volume framework, and this constitutes a major challenge at the moment.

Another interesting direction for future study is the simulation of non-linear phenomena. Finite difference simulations of von Kármán equations have been performed in the past over Cartesian grids [23], but to our knowledge no similar study has been performed over different grids. Such simulations rely on a discrete version of the "triple self-adjointness" property of the non-linear operator [24], which will present new challenges over non-Cartesian grids.

Sound examples and animations from these schemes will be available at:

`http://www2.ph.ed.ac.uk/~s1164563/dafx14.`

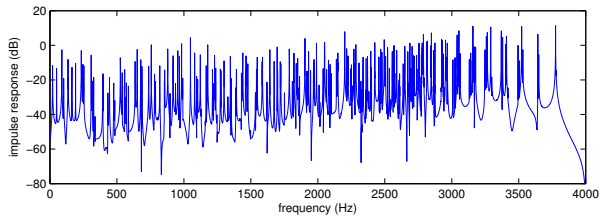

(a) Hexagonal grid, double Dirichlet conditions, $F_s = 8000$ Hz

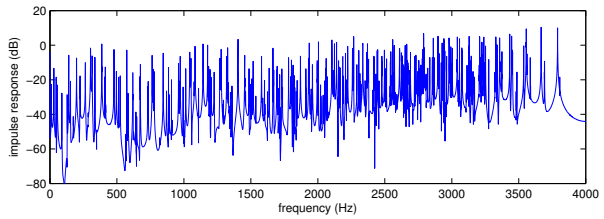

(b) Hexagonal grid, double Neumann conditions, $F_s = 8000$ Hz

Figure 9: Impulse response spectra from circular plate

8. REFERENCES

[1] M. Ducceschi, C. Touzé, and S. Bilbao, "Sound synthesis of gongs obtained from nonlinear thin plates vibrations: Comparison between a modal approach and a finite difference scheme." in *Proc. Stockholm Musical Acoustics Conf. (SMAC)*, Stockholm, Sweden, 2013.

[2] M. Ducceschi, C. Touzé, S. Bilbao, and C. J. Webb, "Nonlinear dynamics of rectangular plates: investigation of modal interaction in free and forced vibrations," *Acta Mechanica*, vol. 225, no. 1, pp. 213–232, 2014.

[3] C. Lambourg, A. Chaigne, and D. Matignon, "Time-domain simulation of damped impacted plates. II. numerical model and results," *J. Acoustical Society of America*, vol. 109, no. 4, pp. 1433–1447, 2001.

[4] S. Bilbao, *Numerical sound synthesis: finite difference schemes and simulation in musical acoustics*. Chichester, UK: Wiley, 2009.

[5] M. van Walstijn and K. Kowalczyk, "On the numerical solution of the 2D wave equation with compact FDTD schemes," in *Proc. Digital Audio Effects (DAFx)*, Espoo, Finland, 2008, pp. 205–212.

[6] B. Hamilton and S. Bilbao, "Hexagonal vs. rectilinear grids for explicit finite difference schemes for the two-dimensional wave equation," in *Proc. Int. Cong. Acoustics (ICA)*, Montréal, Canada, 2013.

[7] S. Bilbao, L. Savioja, and J. O. Smith III, "Parameterized finite difference schemes for plates: Stability, the reduction of directional dispersion and frequency warping," *IEEE Trans. Audio, Speech, and Language Processing*, vol. 15, no. 4, pp. 1488–1495, 2007.

[8] M. Ducceschi, O. Cadot, C. Touzé, and S. Bilbao, "Dynamics of the wave turbulence spectrum in vibrating plates: A numerical investigation using a conservative finite difference scheme," *Physica D: Nonlinear Phenomena*, vol. 280, pp. 73–85, 2014.

[9] L. Collatz, *The numerical treatment of differential equations*, 3rd ed. Berlin: Springer, 1966.

[10] P. Voroshko, "Construction of finite difference diagrams of the engineering theory of elasticity, on the basis of integral representations of the resolvent functions," *Strength of Materials*, vol. 4, no. 8, pp. 943–947, 1972.

[11] J. Tuomela, "Fourth-order schemes for the wave equation, Maxwell equations, and linearized elastodynamic equations," *Numerical Methods for Partial Differential Equations*, vol. 10, no. 1, pp. 33–63, 1994.

[12] D. P. Playne and K. A. Hawick, "Stencil methods and graphical processing units for simulating field," in *Proc. 9th Int. Conf. on Foundations of Computer Science*, 2013.

[13] K. F. Graff, *Wave motion in elastic solids*. Courier Dover Publications, 1975.

[14] S. Timoshenko and S. Woinowsky-Krieger, *Theory of plates and shells*. New York, USA: McGraw-Hill Inc., 1959, vol. 2.

[15] A. H. Nayfeh and D. T. Mook, *Nonlinear oscillations*. New York: John Wiley and Sons, 1979.

[16] S. Bilbao and C. J. Webb, "Physical modeling of timpani drums in 3D on GPGPUs," *J. Audio Engineering Society*, vol. 61, no. 10, pp. 737–748, 2013.

[17] A. Torin and S. Bilbao, "A 3D multi-plate environment for sound synthesis," in *Proc. Digital Audio Effects (DAFx)*, Maynooth, Ireland, 2013.

[18] B. Heinrich, "Boundary value problems and irregular networks," in *Finite Difference Methods on Irregular Networks*. Springer, 1987, pp. 17–39.

[19] S. Bilbao, "Modeling of complex geometries and boundary conditions in finite difference/finite volume time domain room acoustics simulation," *IEEE Trans. Audio, Speech, and Language Processing*, vol. 21, no. 7, pp. 1524–1533, Jul. 2013.

[20] J. Strikwerda, *Finite difference schemes and partial differential equations*. Philadelphia, PA: SIAM, 2004.

[21] C. Meyer, *Matrix analysis and applied linear algebra*. Philadelphia, PA: SIAM, 2000, vol. 2.

[22] A. W. Leissa, *Vibration of Plates*. Washington, D.C.: NASA, 1969.

[23] S. Bilbao, "A family of conservative finite difference schemes for the dynamical von Karman plate equations," *Numerical Methods for Partial Differential Equations*, vol. 24, no. 1, pp. 193–216, 2008.

[24] O. Thomas and S. Bilbao, "Geometrically nonlinear flexural vibrations of plates: In-plane boundary conditions and some symmetry properties," *J. Sound and Vibration*, vol. 315, no. 3, pp. 569–590, 2008.